Optics and Lasers in Engineering 115 (2019) 190–196

Contents lists available at ScienceDirect

Optics and Lasers in Engineering

journal homepage: www.elsevier.com/locate/optlaseng

A two-step calibration method of lenslet-based light field cameras

Ping Zhou*, Weijia Cai, Yunlei Yu, Yuting Zhang, Guangquan Zhou

Southeast University, Sipailou #2, Nanjing 210096, China

ARTICLE INFO

Keywords:
Calibration
Light field
Light field camera
Main lens
Micro-lens array

ABSTRACT

The calibration of lenslet-based light field camera is the key issue to many applications, especially the three-dimensional shape measurement. In this paper, a two-step physically based calibration method is proposed, where every parameter is described with its own physical meaning. The parameters about the main lens of the light field camera are calibrated with the central sub-aperture image, and the parameters about the micro-lens array are calibrated with the epipolar images, subsequently. To improve the calibration result, the distortion correction of the main lens and a nonlinear optimization method are applied also. The calibration method is validated with a commercially available light field camera and compared to Dansereau's calibration method. Typical RMS reprojection errors are 0.0017, 0.0032 mm for 30.0, 35.1 mm calibration grids.

1. Introduction

The light field camera is a novel imaging system that captures direction and location of incoming rays onto the lens, which obtains 3D information of a scene in a single exposure. The prototype of a light field camera was firstly proposed by Adelson and Wang [1] in 1992. Since then, various light field imaging systems, such as camera arrays and lenslet-based (or micro-lens-based) hand-held cameras, were designed. The first commercially available hand-held light field camera was designed by Ng [2,3] in 2005 and then released by Lytro Company. By placing a micro-lens array (MLA) in front of the photo sensor, this camera can estimate angular and spatial information of light rays through it. Because of its low spatial resolution, Lytro camera is called as unfocused light field camera. In 2009, Georgiev and Lumsdaine [4,5] presented a new modified version of Ng's model named focused light field camera, where the MLA is focused on the image formed by the main lens. This system allows to a higher spatial resolution but a lower angular resolution, and it was released by Raytrix. No matter which kind of light field camera, thanks to the rich information captured in a single shot, the application of light field cameras has become a growing area of research. Light field cameras have been used for refocusing [3,6], disparity estimation [7,8], light field panorama [9], visual odometry [10] and Simultaneous Localization and Mapping (SLAM) [11].

As is widely known, in all of these applications, the accuracy and performance can be enhanced if the camera calibration parameters are available. Therefore, the calibration of light field cameras is a key research issue. Different calibration approaches have been proposed. In 2013, Dansereau et al. [12] presented a 15-parameter camera model and method to calibrate unfocused light field cameras. They derived a 4D intrinsic matrix and distortion model which relate the indices of a pixel to its corresponding spatial ray. However, some issues, such as initializing the optimization and resolving calibrated parameters, still exist in their work. In 2014, Bok et al. [13] proposed a new geometrical calibration method of unfocused light field cameras, using line features extracted from the micro-images. However, they didn't model the lens distortion of outer sub-aperture images. Some other methods were presented to calibrate the focused light field cameras. In 2016, Zeller et al. [14] presented a metrical calibration approach, using the totally focused image and virtual depth map to compute 3D observations. The cost function is expressed as the distance between object points and their observations. Nevertheless, their method failed to get feature points for object distance closer than 1 m. Zhang et al. [15] proposed a calibration method based on the relationship between the raw image features and the depth-scale information. Nevertheless, in these works, MLA parameters like its misalignment with the photosensor are not taken into account. To fill this gap, in 2017, Noury et al. [16] presented a calibration method based only on raw images. This work developed a new detector to estimate checkerboard observations directly from raw images with subpixel accuracy. However, they estimated the micro-images grid parameters from white images instead of captured raw images, which introduce uncertainty in calibration process.

In this paper, a practical two-step calibration method of lenslet-based unfocused light field cameras is presented. Instead of estimating a complicated matrix composed of parameters without physical meaning [12,15], the calibration method describes the light field camera parameters with specific physical meaning. Therefore, the calibration model is easy to be understood. The calibration method relates an arbitrary point in space to the indices of a certain micro-lens, and

---

* Corresponding author.
E-mail address: zhouping@seu.edu.cn (P. Zhou).

https://doi.org/10.1016/j.optlaseng.2018.11.024
Received 8 July 2018; Received in revised form 6 November 2018; Accepted 26 November 2018

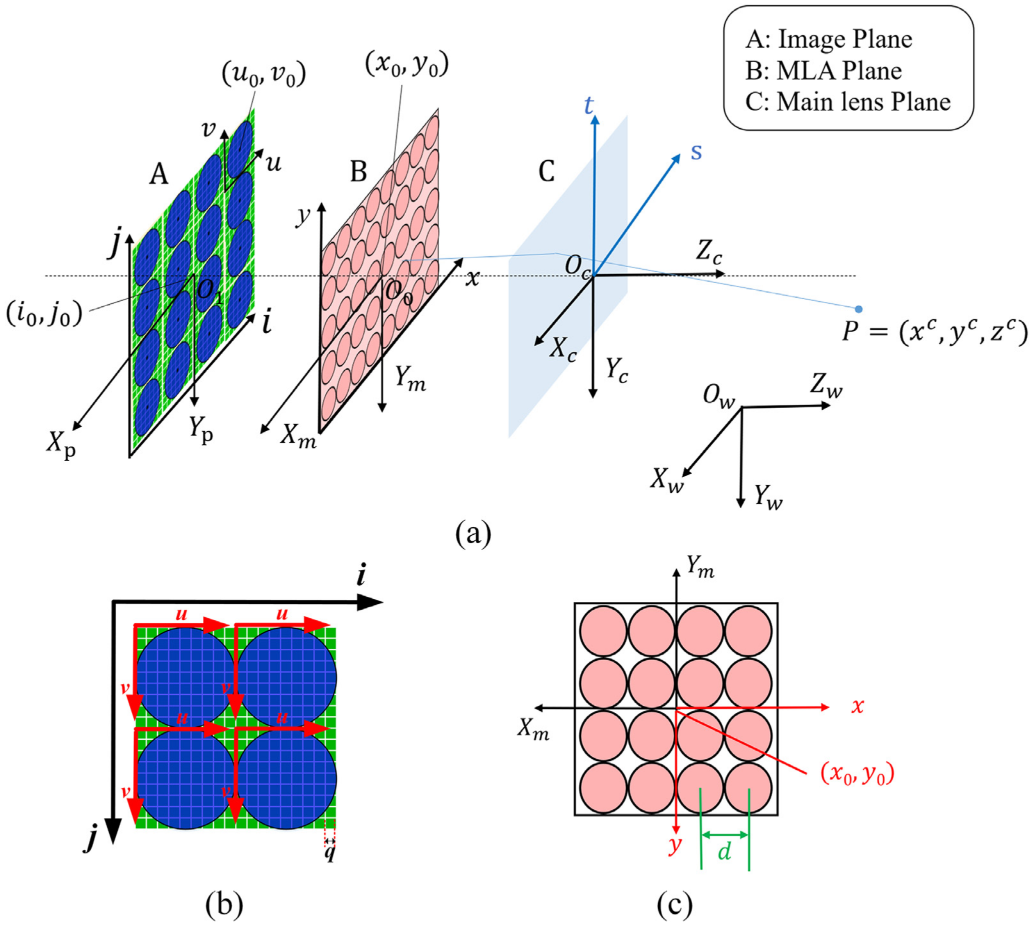

Fig. 1. Geometrical model of light field cameras, (a) Projection model (b) image plane (c) micro-lens plane.

describes the relation between arbitrary point depth and light field disparity subsequently, where the central sub-aperture images and epipolar images are used respectively. Moreover, the distortion of main lens and a nonlinear optimization are also considered to improve calibration performance.

2. Geometrical models of lenslet-based light field cameras

For a lenslet-based light field camera, a geometrical model is proposed based on two-parallel-plane (TPP) model, where the main lens is treated as a thin lens, and the micro-lens as pinholes, similar to [10,14]. An oriented line is defined by connecting a point in one plane to a point in the other plane, expressed as $L(s, t, x, y)$. In this paper, these two planes are the main lens plane (s, t) and micro-lens plane (x, y), which provide the angular and spatial information respectively.

2.1. Projection model

To express the light field ray with TPP model, five coordinate systems are defined as follows: $O_1 - X_pY_p$ is image coordinate system, $O_c - X_cY_cZ_c$ is camera coordinate system, $O_w - X_wY_wZ_w$ is world coordinate and (i, j) is pixel coordinate, as that in the conventional calibration model. In addition, the micro-lens coordinate $O_0 - X_mY_m$ is introduced in this paper. Moreover, in the image plane, (x, y) and (u, v) represent the indices of the micro-images and pixel indices within a micro-image respectively, as depicted in Fig. 1(b). Without loss of generality, the optical center of the main lens and optical axis are defined as the origin O_c and the z_c-axis of camera coordinate, respectively. These planes are parallel to each other and all perpendicular to the optical axis. All coordinate systems follow the same convention: from the observation view (towards right in Fig. 1(a)), the Z axis points towards the object ($Z_C > 0$). The Y axis points downwards and the X axis points to the right. All the coordinates with origins O_x are in the unit of millimeter.

For an arbitrary point on the world focal plane, the Gaussian formula can be expressed as:

$$\frac{1}{h_m} + \frac{1}{h'_m} = \frac{1}{f} \tag{1}$$

where h_m is the distance from the scene point P_0 to the main lens plane, h'_m is the distance from the image plane to the main lens plane, as depicted in Fig. 2, and f is the focal length of the main lens. For convenience, the projection models are simplified to 2D in Figs. 2 and 3, which can be easily generalized to 4D.

The MLA is not shown in Fig. 2 as each sub-aperture image is considered as a perspective image of the scene from the corresponding sub-aperture (s, t) with a virtual photo sensor [17]. The “pixel size” of the virtual photo sensor is the diameter d of micro-lens rather than the original pixel size. The sub-aperture image with $s = u = 0$, $t = v = 0$ is defined as “central sub-aperture image”. As shown in Fig. 2, the relationship between the scene point and the image point is described as follows:

$$\frac{s - x^c}{z^c} + \frac{s - x^m}{h'_m} = \frac{s - x^d}{h_m} + \frac{s - x^m}{h'_m} = \frac{s}{f} \tag{2}$$

where s is the distance from optical center O_c to the sub-aperture of the main lens where the rays pass through it.

From the similar triangles in Fig. 3,

$$D = \frac{qh'_m}{b} \tag{3}$$

$$\begin{aligned} s &= \tfrac{qh'_m(u-u_0)}{b} \\ &= D(u-u_0) \end{aligned} \tag{4}$$

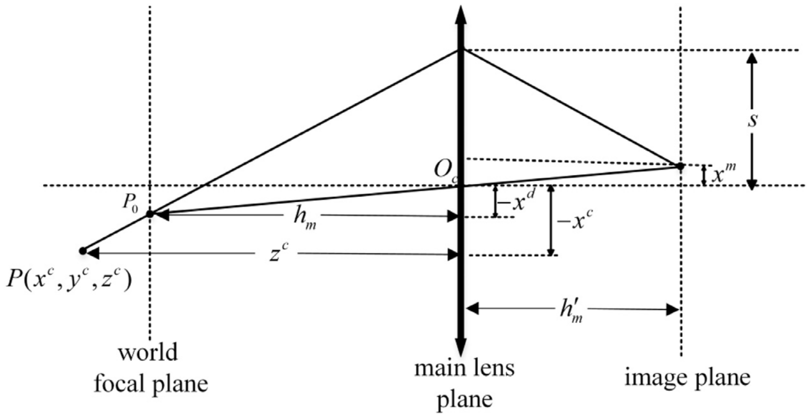

Fig. 2. Projection model without MLA.

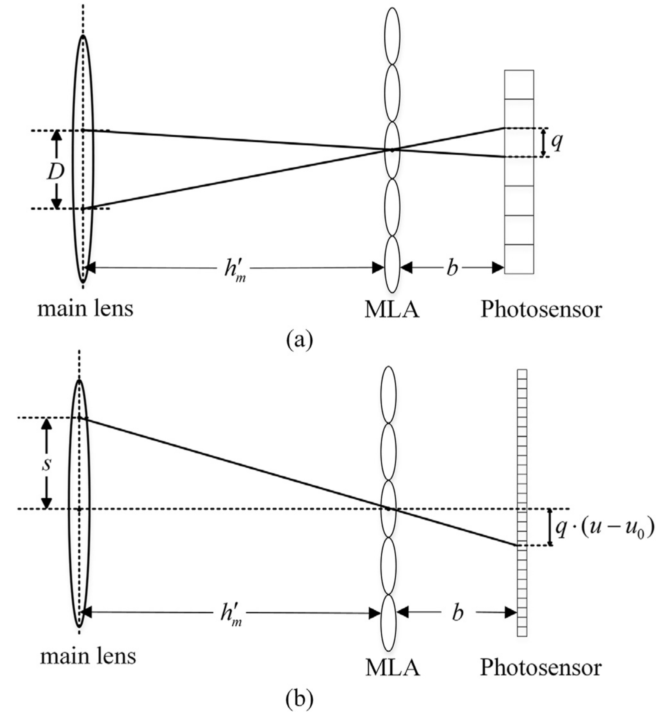

Fig. 3. Light field camera model, (a) the linear relationship between D and q (b) the linear relationship between s and $u - u_0$.

where D is the size of sub-aperture (or synthesized aperture), q is the pixel size, and u is the index of pixels in micro images, as depicted in Fig. 1(b). Eq. (4) shows the linear relationship between s and $u - u_0$.

Let $s_l = D(u_l - u_0)$ and $s_{l+1} = D(u_{l+1} - u_0)$, where l describes the number of pixel index within each micro-image in u direction. s_l and s_{l+1} describe two adjacent sub-apertures, then Eq. (2) is rewritten as:

$$\begin{aligned} \frac{(u_l-u_0)D-x^{m_1}}{h'_m} + \frac{(u_l-u_0)D-x^c}{z^c} = \frac{(u_l-u_0)D}{f} \\ \frac{(u_{l+1}-u_0)D-x^{m_2}}{h'_m} + \frac{(u_{l+1}-u_0)D-x^c}{z^c} = \frac{(u_{l+1}-u_0)D}{f} \end{aligned} \tag{5}$$

Subtracting the top equation from the bottom one in Eq. (5) yields the expression

$$\frac{1}{z^c} = \frac{1}{f} - \frac{1}{h'_m} + \frac{x^{m_2} - x^{m_1}}{Dh'_m} \tag{6}$$

According to Gaussian formula Eqs. (1) and (3), Eq. (6) is described as

$$\begin{aligned} \frac{1}{z^c} &= \frac{1}{h_m} + \frac{-\Delta x \cdot d}{Dh'_m} \\ &= \frac{1}{h_m} + \frac{bd}{qh'^2_m} \cdot (-\Delta x) \end{aligned} \tag{7}$$

where $\Delta x = (x^{m_1} - x^{m_2})/d$, which is the disparity of the scene point P in two adjacent sub-aperture images, and is defined as “light field disparity” in this paper. Based on the theory of epipolar images [18], Δx is unrelated to l, so the light field disparity of any two adjacent sub-aperture images is identical. It can be seen from Eq. (7) that there exists a linear relationship between $1/z^c$ and Δx in single shot. Particularly, when the scene point is in the world focal plane (for example, P_0 in Fig. 2), the light field disparity is zero.

2.2. Lens distortion model

The distortion generated by MLA is ignored in this paper as described in [16,19,20]. The main lens distortion is considered and second-order radial distortion model is expressed in Eq. (8) [21,22].

$$\begin{aligned} x_d &= x_n(1 + k_1 r^2 + k_2 r^4) \\ y_d &= y_n(1 + k_1 r^2 + k_2 r^4) \end{aligned} \tag{8}$$

where $r^2 = {x_n}^2 + {y_n}^2$, k_1,k_2 are radial distortion coefficients of the main lens, (x_d, y_d) are distorted points, (x_n, y_n) are undistorted points, respectively. x_n, y_n are in normalized coordinates, denoted as Eq. (9),

$$\begin{aligned} x_n &= -\frac{x^m}{h'_m} = -\left(\frac{s-x^c}{z^c} - \frac{s}{h_m}\right) \\ y_n &= -\frac{y^m}{h'_m} = -\left(\frac{t-y^c}{z^c} - \frac{t}{h_m}\right) \end{aligned} \tag{9}$$

When $s, t = 0$, the meaning of radial distortion coefficients here is the same to that in Zhang’s model [23].

3. Calibration method

The purpose of light field camera calibration is to determine the accurate relationship between a certain point in world coordinate and some imaging locations in the imaging plane. A two-step calibration method is presented in this paper. First of all, the projection procedures from the world coordinate to the camera coordinate, then to the microlens coordinate are presented, where the central sub-aperture image is applied. Therefore, the calibration is similar to that of the conventional camera. All the intrinsic and extrinsic parameters are estimated by Zhang’s method [23]. According to the classical pinhole model, the relationship between the world coordinate system and the camera coordinate system is shown in Eq. (10).

$$\begin{bmatrix} x^c \\ y^c \\ z^c \\ 1 \end{bmatrix} = \begin{bmatrix} \mathbf{R} & \mathbf{t} \\ 0 & 1 \end{bmatrix} \begin{bmatrix} x^w \\ y^w \\ z^w \\ 1 \end{bmatrix} \tag{10}$$

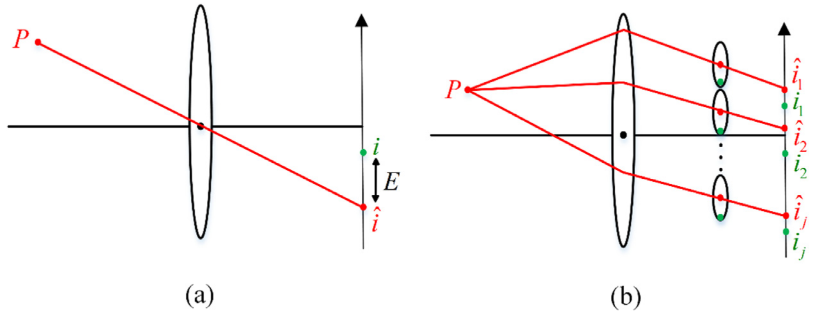

Fig. 4. Reprojection error model, (a) conventional projected calibration (b) light field projected calibration.

Based on Eq. (2), the transformation from camera coordinate system to micro-lens coordinate system is expressed as

$$z^c\begin{bmatrix}x^m\\y^m\\1\end{bmatrix}=\begin{bmatrix}h'_m & 0 & -\frac{sh'_m}{h_m} & -s\cdot h'_m\\ 0 & h'_m & -\frac{th'_m}{h_m} & -t\cdot h'_m\\ 0 & 0 & 1 & 0\end{bmatrix}\begin{bmatrix}x^c\\y^c\\z^c\\1\end{bmatrix} \tag{11}$$

The relationship between (x, y) coordinate and (x^m, y^m) coordinate is expressed as

$$\begin{bmatrix}x\\y\\1\end{bmatrix}=\begin{bmatrix}\frac{1}{d} & 0 & x_0\\ 0 & \frac{1}{d} & y_0\\ 0 & 0 & 1\end{bmatrix}\begin{bmatrix}x^m\\y^m\\1\end{bmatrix} \tag{12}$$

Combining Eqs. (10)–(12) results in the expression

$$\begin{bmatrix}x\\y\\1\end{bmatrix}=\begin{bmatrix}\frac{h'_m}{d} & 0 & x_0-\frac{sh'_m}{dh_m} & -\frac{sh'_m}{d}\\ 0 & \frac{h'_m}{d} & y_0-\frac{th'_m}{dh_m} & -\frac{th'_m}{d}\\ 0 & 0 & 1 & 0\end{bmatrix}\begin{bmatrix}\mathbf{R} & \mathbf{t}\\ 0 & 1\end{bmatrix}\begin{bmatrix}x^w\\y^w\\z^w\\1\end{bmatrix} \tag{13}$$

When the central sub-aperture images are used for calibration, where $s=0, t=0$, Eq. (13) is rewritten as

$$\begin{bmatrix}x\\y\\1\end{bmatrix}=\begin{bmatrix}\frac{h'_m}{d} & 0 & x_0 & 0\\ 0 & \frac{h'_m}{d} & y_0 & 0\\ 0 & 0 & 1 & 0\end{bmatrix}\begin{bmatrix}\mathbf{R} & \mathbf{t}\\ 0 & 1\end{bmatrix}\begin{bmatrix}x^w\\y^w\\z^w\\1\end{bmatrix} \tag{14}$$

It can be seen from Eq. (14) that the goal of the first step calibration is to estimate the extrinsic parameters **R,t** and intrinsic parameters h'_m,(x_0, y_0). In comparison with conventional camera projection model, d is the diameter of the micro-lens, which is the pixel size of virtual photo sensor instead of the realistic pixel size. Although the model in this paper substitutes central sub-aperture image for the convention camera, the calibration principles are still identical. Therefore, the extrinsic and intrinsic parameters of the main lens are derived based on Zhang's calibration method [23].

Except for the parameters about the main lens, some other parameters such as the distance D between the centers of two adjacent sub apertures, the distance b between MLA and photo sensor, and object distance h_m are calibrated subsequently. For each feature point in sub-aperture images, the depth z_c and light field disparity Δx are derived based on extrinsic parameters and epipolar images, respectively. Eq. (7) shows the constraint between z_c and Δx, and Eq. (3) shows the constraint between b and D. Therefore, these parameters b,D and h_m are derived with line fitting method.

Finally, a nonlinear optimization approach is employed to refine these parameters and improve the precision. For conventional calibration, a feature point P corresponds to a certain point in the image plane, as shown in Fig. 4(a), and the Euclidean distance from observed to expected projected feature locations is denoted as "reprojection error", expressed as $|E| = |i - \hat{i}|$. However, it's much more complicated in light field camera calibration as a feature point appears multiple times in the image plane, as shown in Fig. 4(b). Therefore, a feature point has several reprojection error, which is expressed as $|E_j| = |i_j - \hat{i}_j|$.

In light field cameras, the observed feature points are extracted from an array of $N_u \times N_v$ sub-aperture images, the calibration board is captured at M different angles, and there are n_c calibration feature points on each calibration board. Therefore, the goal of optimization is to find out the parameters $\mathbf{R}, \mathbf{t}, h'_m, x_0, y_0$, distortion vector $\mathbf{k} = (k_1, k_2)$, the depth of world focal plane h_m, and sub-aperture size D, which minimize the error across all features, as expressed in Eq. (15).

$$\mathop{\arg\min}_{\mathbf{R},\mathbf{t},\mathbf{k},h_m,h'_m,x_0,y_0,D}\ \sum_{c=1}^{n_c}\sum_{m=1}^{M}\sum_{s=1}^{N_u}\sum_{t=1}^{N_v} E^{s,t}_{m,c}\left(\mathbf{R},\mathbf{t},\mathbf{k},h_m,h'_m,x_0,y_0,D\right) \tag{15}$$

As shown in Eq. (15), the optimization is a nonlinear least squares problem. The Levenberg–Marquardt algorithm is applied in our calibration procedure. To avoid being trapped in local minima, the appropriate initial values are given to the optimization [22], which are close to the optimal calibration results. In addition, as the genetic algorithm could achieve the calibration without initial values [24,25], it is applied in the optimization to compare with Levenberg–Marquardt algorithm and the same calibration accuracy is obtained. As the initial values are easy to be computed in the calibration, the Levenberg–Marquardt algorithm is applied in the end.

The specific implementation steps of the calibration method proposed in this paper are summarized as follows:

STEP 1: A light field camera is used to acquire images of calibration board at Mdifferent angles. The calibration board is placed in front of and behind the focused plane for calibration.
STEP 2: The raw 2D images are decoded to a 4D light field representation. Subsequently, the sub-aperture images and epipolar images are derived from the 4D representation.
STEP 3: Using Mcentral sub-aperture images, the intrinsic and extrinsic parameters of the main lens in Eq. (14) are calibrated by Zhang's calibration method [23].
STEP 4: Extracting the feature points in all sub-aperture images and computing the light field disparity Δx.
STEP 5: The feature points in camera coordinate system are obtained from the world coordinate based on the extrinsic matrix.
STEP 6: For each feature point in STEP 5, its depth $z^c$is obtained according to calibration results in STEP3, and its corresponding light field disparity $\Delta x$is obtained in STEP4. Therefore, the coefficients about MLA in Eq. (7) are calibrated with least square fitting method.
STEP 7: Nonlinear optimization.

4. Experiments and results

The light field camera, Lytro Illum, was used to verify the proposed method. The experimental vision system to perform the calibration is shown in Fig. 5, including a light field camera, a calibration board and a computer. To extract sub-aperture images and epipolar images, the 4D light field $L(s, t, x, y)$ is recovered from the original 2D image

Fig. 5. Light field camera setup to perform calibration.

Table 1
Parameters of the light field camera before and after optimization.

	Parameters	Initial values	Optimized values
Central sub-aperture images calibration results	h'_m (mm)	65.1261	64.8052
	(x_0, y_0) (pixel)	(321.6482, 236.3598)	(321.3414, 239.0053)
	$\mathbf{R}$ ($\times10^{-3}$rad)	(−0.0313, −0.0444, −0.0182)	(−0.0328, −0.0408, −0.0181)
	$\mathbf{t}$(mm)	(−100.0919, −119.0575, 2553.2)	(−99.8769, −120.8548, 2542.1)
	(k_1, k_2)	(0.2235, 30.8967)	(0.3995, −1.5771)
Line fitting results	D (mm)	1.8922	1.8668
	b (mm)	0.0482	0.0477
	$\mathrm{h_m}$ (m)	2.7122	2.7015

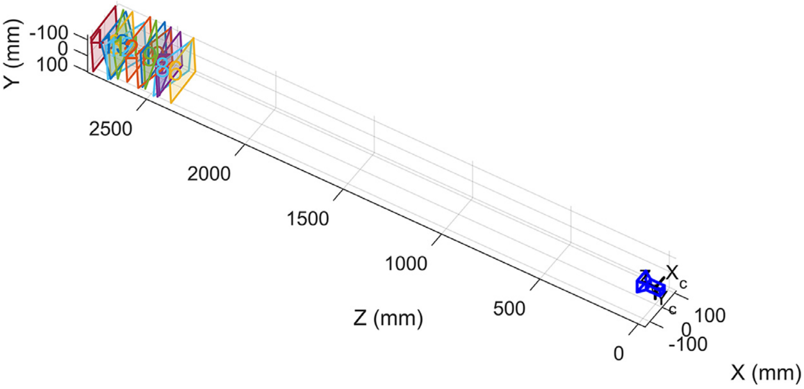

Fig. 6. Results of the positions of the light field camera and the calibration board.

recorded on the photo sensor, where the MATLAB toolbox LFToolbox V0.4 designed by Dansereau et al. [12] is used. The 4D light field includes 15 × 15 array of sub-aperture images with 625 × 434 pixels. In experiments, a calibration board with circular patterns was captured at $M = 13$ perspectives, which is placed about 2000 mm away from the main lens of the light field camera. The nominal distance between adjacent circular centers of the calibration board is 30.00 mm. The 35 mm equivalent focal length of the main lens is 30 mm, the pixel size of q is 0.0014 mm, and the distance of d between adjacent micro-lens after decoding is 0.01732 mm, which are obtained from the metadata provided by Lytro. The calibration results of the light field camera are detailed in Table 1, and the positions of the light field camera and the calibration board at M perspectives are shown in Fig. 6.

To calibrate the parameters about the MLA, the epipolar images are derived from the decoded light field $L(s, t, x, y)$. Every center of the circles is derived by the methods developed in our previous works, and every slope k of the straight lines in epipolar images is derived by line fitting method, which are formed by corresponding circle centers in different sub-aperture images. Therefore, the light field disparity of $\Delta x = 1/k$ in Eq. (7) is derived. Each feature point in world coordinate (x^w, y^w, z^w) is converted to camera coordinate (x^c, y^c, z^c), using the extrinsic parameters. Subsequently, the linear relationship between $1/z_c$ and Δx expressed in Eq. (7) is retrieved, as shown in Fig. 7. The fitting line is $1/z_c = 1.4055 \times 10^{-4} \cdot \Delta x + 3.6871 \times 10^{-4}$, and the norm of the residuals

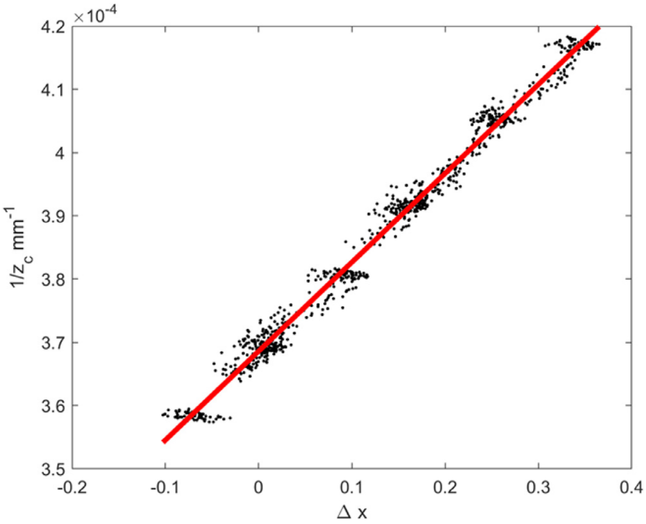

Fig. 7. The fitting line of Eq. (7).

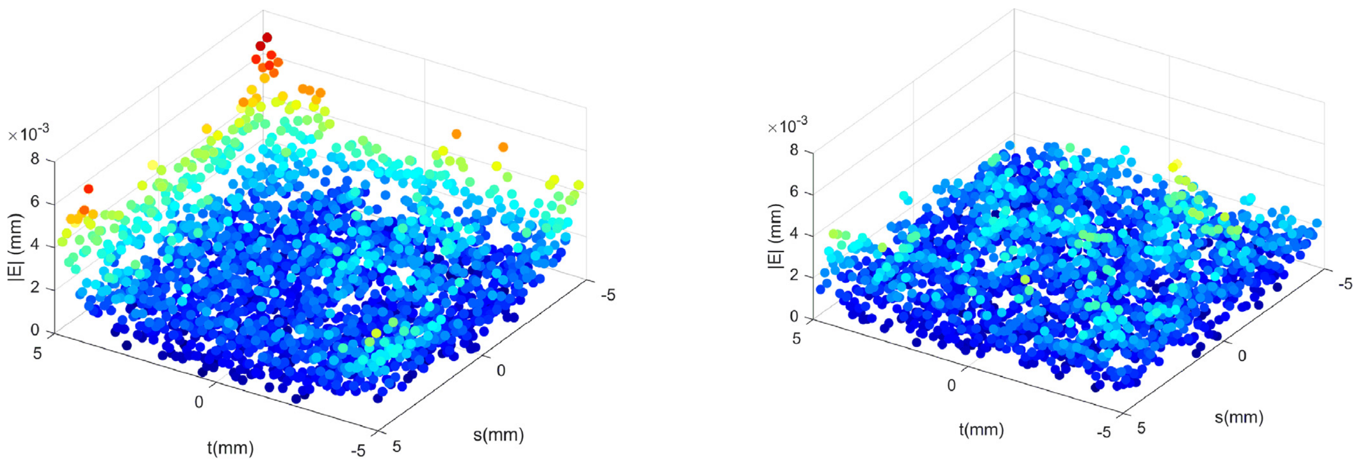

(a) (b)

Fig. 8. Reprojection error for 30.0 mm grid, (a) without nonlinear optimization and distortion correction; (b) with nonlinear optimization and distortion correction.

Table 2
RMS of Ray Reprojection Error (mm).

	Dansereau’s method			Our method	
Grid	3.61	7.22	35.1	30.0	35.1
RMS	0.0628	0.105	0.363	0.0017	0.0032

is 6.022×10^{-5}. According to the fitting line coefficients of Eq. (7) and Eq. (2), the parameters about MLA, D, b and h_m are computed, as depicted in Table 1. All these results are used as the initial values, then the nonlinear optimization is applied to increase the calibration accuracy. Therefore, light rays in the light field can be traced after calibration, according to the parameters about the main lens and MLA.

The reprojection error of the proposed model before and after nonlinear optimization and distortion correction is shown in Fig. 8. In Fig. 8(a), the reprojection error on the margin of the main lens is larger than that in the middle of the main lens, while the reprojection error after optimization and correction is identical approximately, as shown in Fig. 8(b). The calibration results are compared to that proposed by Dansereau et al. [12], as depicted in Table 2. The distance between adjacent feature points is expressed as “grid”. With Dansereau’s method, typical RMS ray reprojection errors are 0.0628, 0.105, 0.363 mm for 3.61, 7.22, 35.1 mm calibration grid, as shown in column 2–4, Table 2. It can be concluded that the calibration board with a smaller grid size will have a higher accuracy. Typical RMS ray reprojection errors are 0.0017, 0.0032 mm for 30.0, 35.1 mm calibration grids in our experiments, which are smaller than the results in Dansereau’s paper. The reprojection error demonstrates that the geometrical models of the lenslet-based light field camera and the calibration method proposed in this paper work well. Furthermore, to demonstrate the measurement accuracy, the distance of circle pairs in the calibration board is measured, whose nominal grid size of 30.00 mm is used as the ground truth. The RMS of the measurement error is 0.288 mm and the relative error is 0.96%.

5. Conclusion

A practical calibration model and method for lenslet-based light field camera are presented in this paper. The projection model from a scene point to the indices of a certain pixel was derived, which includes the relationship between the depth and light field disparity. The distortion correction for the main lens and the nonlinear optimization based on ray reprojection were presented also. Validation was performed and the typical RMS ray reprojection errors are 0.0017, 0.0032 mm for 30.0, 35.1 mm calibration grids. Although Donald’s 15-parameter camera model is of lower dimensionality, the parameters are lack of physical meanings, so that it is much more difficult to be understood than the model proposed in this paper. Furthermore, there is an arbitrary plane as (*u*, *v*) plane in their model, which separates from the main lens with an unknown distance *D*, while *D* is difficult to be determined in applications. Future work includes a more complicated lens distortion model, improving the accuracy of light field disparity, and overcoming the limitations of pinhole and thin lens models.

Reference

[1] Adelson EH, Wang JY. Single lens stereo with a light field camera. IEEE Trans Pattern Anal Mach Intell 1992;14(2):99–106.
[2] Ng R, et al. Light field photography with a hand-held light field camera. Comput Sci Tech Rep 2005;2(11):1–11 CSTR.
[3] Ng R. Digital light field photography. Stanford University; 2006.
[4] Georgiev T, Lumsdaine A. Rich image capture with light field cameras. In: 2010 IEEE international conference on computational photography (ICCP); 2010. p. 1–8.
[5] Georgiev T, Lumsdaine A. Reducing light field camera artifacts. Comput Graph Forum 2010;29:1955–68. doi:10.1111/j.1467-8659.2010.01662.x.
[6] Levoy M. Light fields and computational imaging. Computer 2006;39(8):46–55.
[7] Tao MW, Hadap S, Malik J, et al. Depth from combining defocus and correspondence using light-field cameras. In: 2013 IEEE international conference on computer vision (ICCV). IEEE; 2013. p. 673–80.
[8] Wanner S, Goldluecke B. Globally consistent depth labeling of 4D light fields. In: 2012 IEEE conference on computer vision and pattern recognition (CVPR). IEEE; 2012. p. 41–8.
[9] Birklbauer C, Opelt S, Bimber O. Rendering Gigaray light fields. In: Computer graphics forum, 32 (2pt4). Blackwell Publishing Ltd; 2013. p. 469–78.
[10] Dansereau DG, Mahon I, Pizarro O, et al. Light field flow: closed-form visual odometry for light field cameras. In: 2011 IEEE/RSJ international conference on intelligent robots and systems (IROS). IEEE; 2011. p. 4455–62.
[11] Dong F, Ieng SH, Savatier X, et al. Light field cameras in real-time robotics. Int J Robot Res 2013;32(2):206–17.
[12] Dansereau DG, Pizarro O, Williams SB. Decoding, calibration and rectification for lenslet-based light field cameras. In: IEEE computer society conference on computer vision and pattern recognition; 2013. p. 1027–34.
[13] Bok Y, Jeon HG, Kweon IS. Geometric calibration of micro-lens-based light field cameras using line features. IEEE Trans Pattern Anal Mach Intell 2017;39(2):287–300.
[14] Zeller N, Noury CA, Quint F, et al. Metric calibration of a focused light field camera based on a 3D calibration target. ISPRS Ann Photogrammetry Rem Sens Spat Inf Sci 2016;3:449.
[15] Zhang C, Ji Z, Wang Q. Decoding and calibration method on focused light field camera. Comput Vis Media 2016;2(1):57–69.
[16] Noury CA, Teuliere C, Dhome M. Light-field camera calibration from raw images. In: 2017 international conference on digital image computing: techniques and applications (DICTA). IEEE; 2017. p. 1–8.
[17] Zhou Z, Yuan Y, Bin X, Qian L. Super-resolved refocusing with a light field camera. In: Proceedings of the SPIE 7873, computational imaging IX, 787313; 2011 8 February.
[18] Bolles RC, Baker HH, Marimont DH. Epipolar-plane image analysis: an approach to determining structure from motion. Int J Comput Vis 1987;1(1):7–55.
[19] Mouroulis P, Macdonald J. Geometrical optics and optical design. Oxford Series in Optical & Ima; 1997.

[20] Fischer RE, Tadic-Galeb B, Yoder PR, et al. Optical system design. New York: McGraw Hill; 2000.

[21] Duane CB. Close-range camera calibration. Photogramm Eng 1971;37(8):855–66.

[22] Zhang Z, Matsushita Y, Ma Y. Camera calibration with lens distortion from low-rank textures. In: 2011 IEEE conference on computer vision and pattern recognition (CVPR). IEEE; 2011. p. 2321–8.

[23] Zhang Z. A flexible new technique for camera calibration. IEEE Trans Pattern Anal Mach 2000;22(11):1330–4.

[24] Rodríguez JAM, Mejía Alanís FC. Binocular self-calibration performed via adaptive genetic algorithm based on laser line imaging. J Mod Opt 2016;63(13):1219–32.

[25] Rodríguez JAM. Microscope self-calibration based on micro laser line imaging and soft computing algorithms. Opt Lasers Eng 2018;105:75–85.